Original article

Textile Research Journal

Textile Research Journal
0(00) 1–24

DOI: 10.1177/0040517511398944
trj.sagepub.com

SAGE

Characterization of the tensile behavior of a metallic fiber woven structure

Steven M Kraft and Ali P Gordon

Abstract

The mechanics of a woven wire mesh material are investigated to characterize the elasto-plastic behavior of this class of materials under tensile conditions. The study focuses on a representative 316 L stainless steel (316 L SS) 325 × 2300 twill-dutch woven wire mesh typically used as a fine filtration media in applications such as water reclamation, air filtration, and as a key component in swab wands used in conjunction with explosive trace detection equipment. Mechanical experiments and a 3D finite element model were employed to study the macro-scale and meso-scale mechanical behavior of the woven wire mesh under uniaxial tensile conditions. A parametric study of the orientation dependence of the mechanical response of this material has been carried out, which relates material properties such as elastic modulus, yield strength, etc. to material orientation. Ratcheting type tensile tests are also performed in a similar orientation study, and an elementary damage model is presented for the woven wire mesh based on continuum damage mechanics. The elasto-plastic behavior of the wire mesh is studied via the finite element method, and observations are made relating localized plastic strain to remotely applied displacements.

Keywords

Resilience, Hill's analogy, Voce hardening model

Introduction

Composite material mechanics is a thriving research field, stemming from the need for lightweight and high-strength materials selected for numerous cutting edge applications. The study of composites is generally classified into three scales: the micro, meso, and macro-scale. The micro-scale considers microstructural details such as surface defects or micro-cracks, and is not dealt with in the current study. The meso-scale is comprised of some representative volume element (typically one full weave period for fabrics) that captures component level interaction, while the macro-scale is representative of specimen sized sample behavior. Until recent advancements in numerical modeling techniques (i.e. homogenous plates and bricks), this research was restricted to idealized simple structures and somewhat limited mechanical tests (e.g. uniaxial tensile). More recently, analyses of the mechanical behavior of intricate composites have been performed in great detail using the finite element method and other numerical techniques. Geometrically accurate meso-scale finite element models (FEMs) are commonly employed in the literature to study various wire interactions and failure modes.[1–4] These previous modeling efforts have proven the finite element method quite capable of capturing the behavior of this class of materials; however, the high computation expense of meso-scale modeling has lead to idealized contact definitions and reduced model sizes in the literature, ultimately affecting the performance of these models.

Pierce first addressed the modeling of woven textiles in 1936[5] by proposing a simple geometric model for a plain weave fabric that formed the basis of several mechanical models in future works. The geometry of Pierce has been used in several cases to develop numerical models for the study of fabric behavior, most

Department of Mechanical, Materials, & Aerospace Engineering, University of Central Florida, USA.

Corresponding author:
Steven M. Kraft, Department of Mechanical, Materials, & Aerospace Engineering, University of Central Florida, Orlando, FL 32816-2450, USA
Email: kraftsm@knights.ucf.edu

notably in the case of Tarfoui and co-authors.[2] Their work employed the Pierce geometric model in a 'fundamental cell' FE model. This model was used to facilitate damage prediction in the form of yarn breakage. Similar to the Pierce model, Kawabata[6] proposed a meso-scale model in 1964 that made use of a simplified geometry to study the biaxial deformation of plain weave fabrics. He treated the fabric yarns as simple beam like structures, imparting loads on each other at a single cross over point in the plane of the weave. King and co-authors[7] utilized a modified Kawabata geometry, adding axial and rotational springs at the contact points to simulate wire interaction. This model presents a means to predict macro-scale behavior based on the weave geometry and yarn (or wire) materials through a simplification that treats the weave as a homogenized anisotropic body. Such simplification of fabric geometry is common throughout the literature,[7,8] but is typically made after significant numerical modeling or mechanical testing has been performed to formulate the material response, as is the case in the work presented here. After an exhaustive literature search, no models have been found that simulate the wire scale response of such a tortuously dense fabric at the meso-scale as is proposed in the current study; furthermore, little attention has been paid to the elasto-plastic region of the load-deflection curve. The developed model avoids uncertainty in wire interaction by utilizing frictional wire contact definitions, and contains several more weave periods than other models found in the literature to assure the mechanical response is not dominated by the imposed boundary conditions.

Thorough mechanical testing of the 325×2300 woven wire mesh has also been carried out to characterize orthotropic behavior of this material. The ASTM standard D4964 (2008) gives guidelines for the tension testing of elastic fabrics. The standard specifies a constant rate of extension (CRE) type test is to be used. The most common forms of testing in the literature are uniaxial and biaxial tension tests, typically performed at various material orientations. Kumazawa and coworkers[9] performed biaxial tests on plane stress cruciform specimens, and uniaxial tension tests on strip specimens. Chen and colleagues[10] performed uniaxial tensile tests on coated fabric specimens in several material orientations to determine the anisotropic mechanical behavior of the material. Perhaps the most sophisticated experimental setup present in the literature is proposed by Cavallaro and co-workers.[1] Their testing mechanism, referred to as a 'combined multi-axial tension and shear test fixture', is capable of providing stiffness results both in shear and in multi-axial tension tests.

This paper presents research conducted to characterize the mechanical behavior of 325×2300 316 L SS woven wire mesh subject to uniaxial tensile conditions. Data from CRE experiments is presented, and various mechanical properties of the material are classified. An orientation study of the mechanical properties is performed, and models are proposed. The Voce hardening model[11] is employed to characterize the elasto-plastic region of the tensile test results. Ratcheting type tensile test data is presented and analyzed, and an orientation dependent continuum damage model is proposed. Finally, 3D FEM is employed to investigate the meso-scale response of the woven mesh.

The woven wire mesh

The woven wire mesh has a long history of use as a filtration media in industry. Its ability to withstand relatively large pressures while still maintaining extremely high particle retention rates makes it an excellent choice for water reclamation applications. Most recently, this class of materials has been employed in explosive trace detection (ETD) devices, where its ability to sustain repeated thermal shock under high stress is key. The twill-dutch woven specimen of interest is an extremely dense and tightly woven fabric, with nominal and absolute pore sizes of 2 and 7 microns, respectively. Twill refers to the over-two, under-two weaving of the weft wires with respect to the warp wires, while the term dutch implies that the weft wires are smaller in diameter than the warp wires. The woven mesh specifications are defined in Figure 1a, and summarized in detail in Table 1. Approximate crimp radius of curvature values are also provided in Figure 1a, with ρ_1, the radius in the t-weft plane, equal to 0.002 in (0.051 mm), and ρ_2, the radius in the warp-weft plane, equal to 0.005 in (0.127 mm). The given wire diameters are as reported by the manufacturer, and may vary within their tolerance limits. ASTM standard E2016 (2006) provides equations to analytically arrive at the reported mesh weight and thickness values.

The wire material in the representative woven mesh is 316 L SS, chosen for its corrosion resistance, toughness, resistance to temperature variation, and strength. The material properties of AISI for this material are provided in Table 2.[12] It should be noted, however, that the material properties of the actual wires making up the woven mesh may strongly differ from unprocessed 316 L SS. A significant amount of processing during drawing and weaving causes considerable cold working of the wires, undoubtedly affecting their properties to some degree. Evidence of this may be observed from scanning electron microscopy (SEM) images taken of the sample specimens in Figure 2. It is clearly shown that the weaving process causes areas of residual deformation in as-received samples. For the current study, residual deformation and stresses are

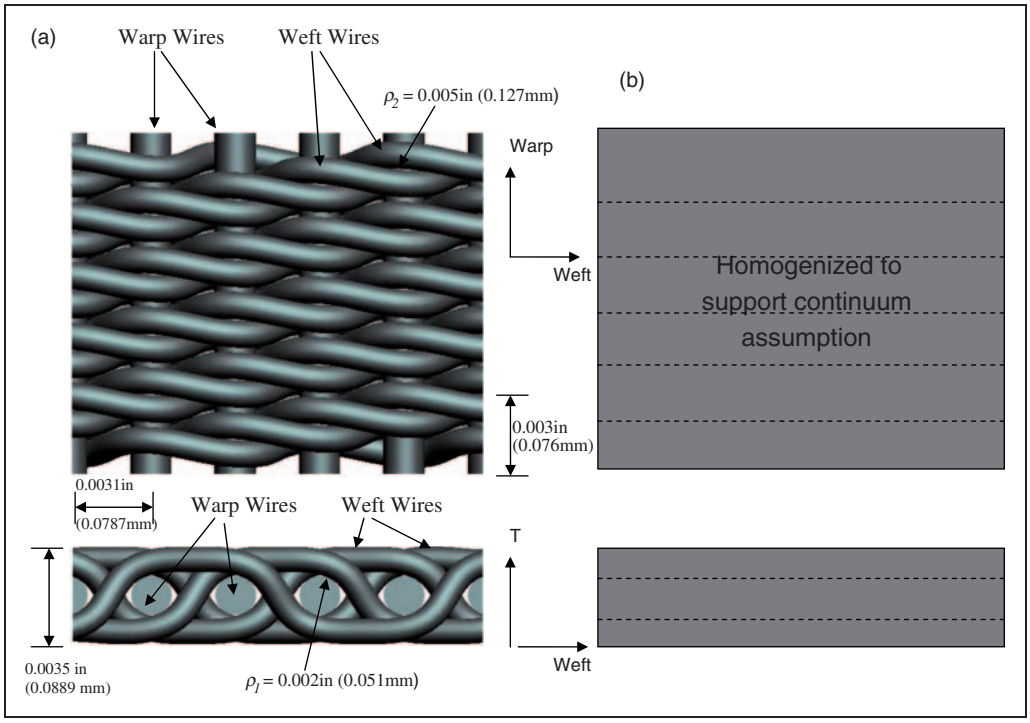

Figure 1. a) Schematic representation of 316 L stainless steel 325 × 2300 woven wire mesh, b) continuum representation of woven wire mesh.

Table 1. 325 × 2300 316 L SS woven wire mesh specifications

Units	Warp wire count, N_s	Weft wire count, N_w	Warp wire diameter, D_s	Weft wire diameter, D_w	Mesh thickness, T	Mesh weight, W
English	325 wires/in	2300 wires/in	0.0015 in	0.0010 in	0.0035 in	0.099 lb/ft^2
SI	127 wires/cm	905 wires/cm	0.0381 mm	0.0254 mm	0.0889 mm	483.4 g/m^2

Table 2. Material properties of Stainless steel 316 L wire at room temperature[12]

Units	Elastic modulus, E	Yield strength, s_y	Ultimate tensile strength, UTS	Density, ρ	Elongation (%)	Poisson's ratio, ν
SI	193 GPa	205 MPa	520 MPa	0.008 *g/mm*^{3}	40	0.28
English	28.0 Msi	29.7 ksi	75.4 ksi	0.289 *lbf/in*^{3}	40	0.28

ignored, and wires are assumed to have homogenous properties.

Tensile experiments

The ASTM standard D4964 (2008) provides guidelines for the mechanical testing performed on the woven wire mesh. The mechanical response of the woven wire mesh was determined by means of CRE tensile testing at a rate of 0.10 in/min (2.54 mm/min) for all cases. Mechanical properties such as stiffness, yield strength, ultimate tensile strength, toughness, rupture strength, and elongation to failure could all be determined from one test. An electromechanical universal testing machine (MTS Insight 5) was applied for this endeavor. Several series of experiments were carried out until samples completely ruptured, as shown in Figure 3.

Single wide specimens

The single wide test specimens were incised to the typical dog-bone shape according to the specimen

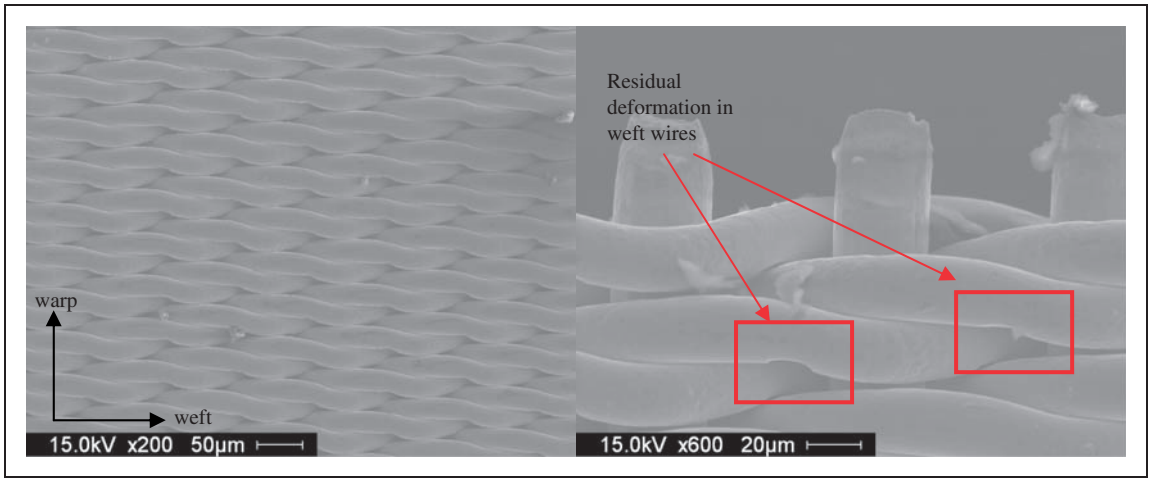

Figure 2. Scanning electron microscope images of the 316 L stainless steel 325 × 2300 woven wire mesh showing residual deformation caused by the weaving process.

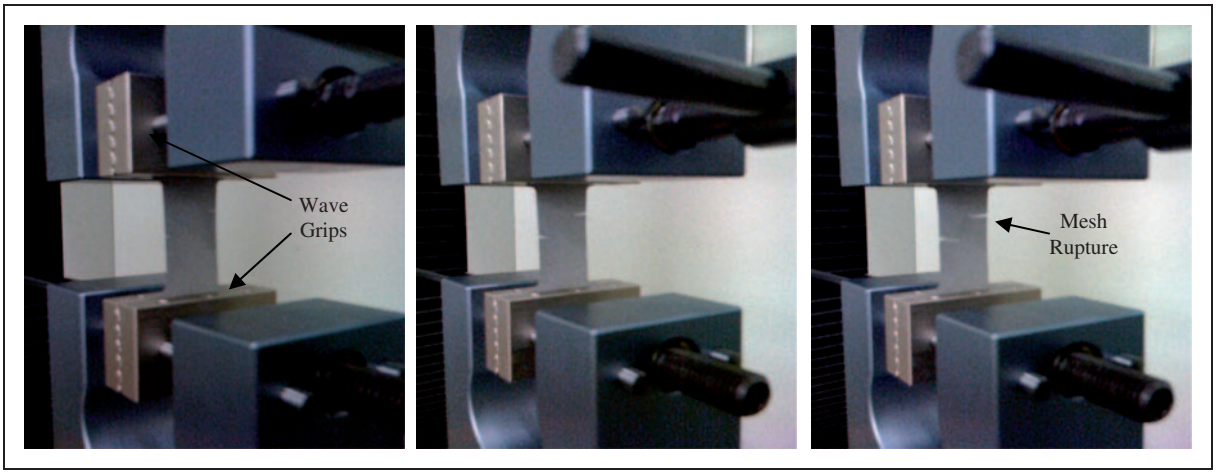

Figure 3. Time-lapse photography of CRE tensile test conducted on 316 L stainless steel 325 × 2300 mesh specimens in the warp (0°) orientation.

drawing shown in Figure 4. The specimen shape was iteratively designed like a conventional test specimen (ASTM E8, 2004) so that failure occurred between the grips and away from the filleted sections of the sample. The results proved exceptionally reproducible in a vast majority of the experiments, with failure typically occurring away from the filleted grip ends as intended. Test specimens were fixed into place with a set of screw vice grips rated at 1.1 kip (5 kN). Each specimen featured a wave grip appropriate for testing thin and potentially difficult to grasp materials (e.g. bituminous, biomaterials, or geo-textiles). The mechanical grips (Test Resources model G86G), shown in Figure 3, were aligned to impart axial loading without twist to the sample.

The orientation dependence of the material was investigated by conducting identical CRE experiments on samples that differed by orientation. Specimens were incised from the mesh sheets at intermediate orientations between the warp (0°) and weft (90°) axes in increments of 15°. In this manner, the mechanical properties of the warp and weft axes serve as a benchmark for the off-axis orientations.

Double wide specimens

As the woven wire mesh is incised at orientations increasingly off the main material axes (i.e., 30°, 45°, 60°), a certain degree of wire 'cut-off' is unavoidable.[9] Consequently, several wires cannot fully participate in carrying the applied load during an off-axis tensile test,

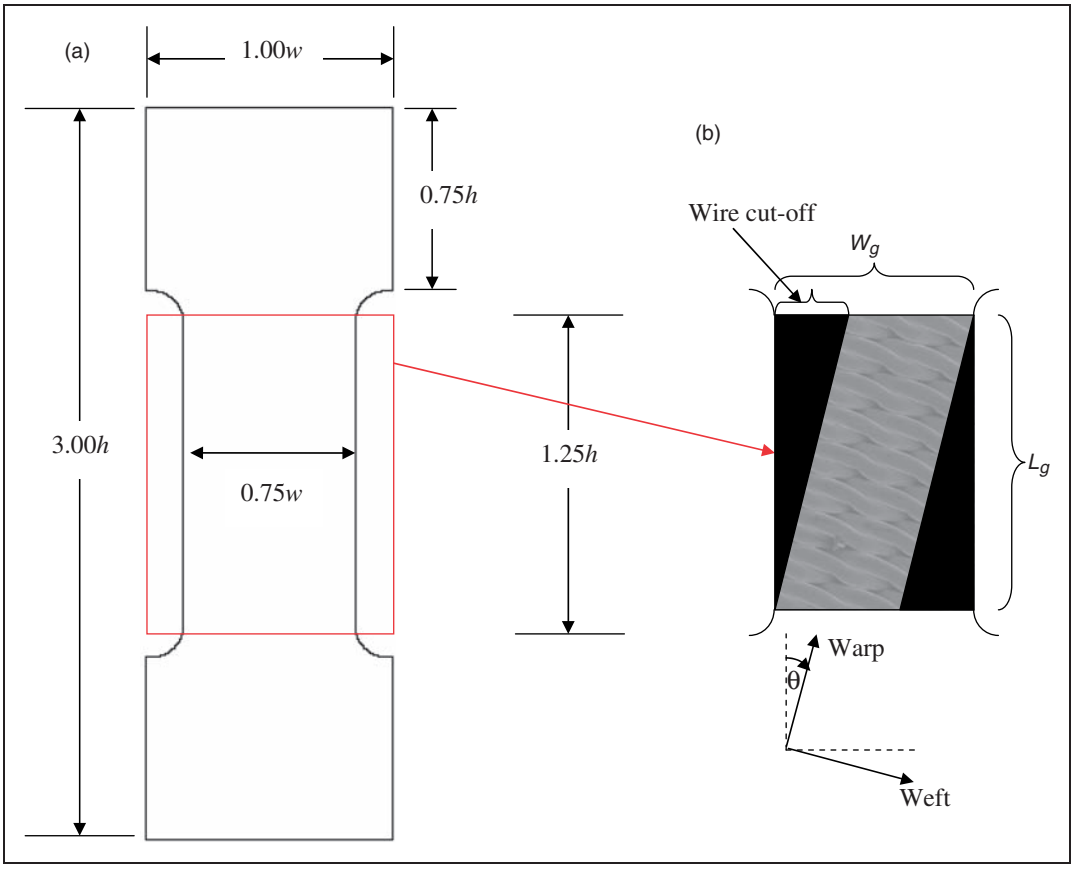

Figure 4. a) Sketch of the incised test specimen used for tensile experiments of the 316 L stainless steel 325 × 2300 woven wire mesh; $w = 1.00$ in (25.4 mm) for single wide and 2.00 in (50.8 mm) for double wide specimens, $h = 1.00$ in (25.4 mm) for all specimens; b) gauge section of the tensile test specimens.

as is illustrated in Figure 4b. To investigate how this reduction in gauge-to-gauge wire count affects the mechanical response of the woven wire mesh, double wide specimens were incised and tested in a similar manner to the single wide specimens. To broaden the scope of data collected from the double wide specimens, resilience type tensile testing, in which the specimens were subjected to alternating ratcheting cycles at various material orientations, was employed. These tests provided load-deflection information similar to the single wide CRE type tensile experiments, hence conventional mechanical data could be obtained, as well as an insight into the damage evolution and hysteresis of the 316 L SS woven wire mesh.

In order to quantify the effectiveness of the double wide samples in alleviating wire cut-off, an equation relating the shank-to-shank wire count, N', to the orientation angle, θ, ranging from 0° to 90°, is required, for example,

$$N'_w = \max\{0, \quad N_w[W_g - L_g \tan(\theta)]\} \qquad (1a)$$

$$N'_s = \max\{0, \quad N_s[W_g - L_g \tan(90^\circ - \theta)]\} \qquad (1b)$$

Here, L_g is the specimen gauge length, W_g is the specimen gauge width, N'_w is the shank-to-shank warp wire count after incision, N'_s is the shank-to-shank shute (or weft) wire count after incision, N_w is the original warp wire count pre-incision, and N_s is the original shute (or weft) wire count pre-incision. Using this relation, the degree of wire cut-off upon incision may be analytically determined. It can be shown that increasing the width of the sample effectively reduces the number of affected wires. For example, 30° oriented samples of the current study have fully active warp and weft counts of 9 and 0 for single wide, and 253 and 0 for double wide samples, respectively.

Experimental results and discussion

The main weave directions, referred to as the warp ($\theta = 0^\circ$) and the weft ($\theta = 90^\circ$) as illustrated in Figure 1, serve as clear points of reference for the

Table 3. Normalized mechanical properties of 316 L SS woven wire mesh in warp direction

Specimen ID	Cross-sectional area, A/A_0	Stiffness, k/k_0	Yield strength, S_y/S_{y0}	Ultimate strength, UTS/UTS_o	Fracture stress, S_f/S_{f0}	Elongation, $\in_f/\in_{f0}$
AR-001	1.00	1.00	0.95	1.00	1.00	1.00
AR-002	1.01	0.96	0.89	0.97	1.00	0.92
AR-003	1.01	1.08	0.98	0.98	1.00	1.04
AR-004	0.99	1.17	1.00	1.03	1.00	1.13
AR-005	0.99	1.25	0.96	1.01	1.01	0.83
AR-006	0.99	1.05	0.96	1.03	0.98	1.13
AR-007	0.99	1.24	0.97	1.01	0.98	1.04
AR-008	1.00	0.99	1.01	1.01	0.99	1.11
AR-009	0.99	1.17	0.98	1.04	1.00	1.08
AR-010	1.00	1.05	1.02	1.03	0.98	1.25

classification of the tensile behavior of the 325×2300 316 L SS woven wire mesh. The main orientations represent the only cases where pure tensile conditions can be produced via uni-axial tensile tests on the woven mesh due to the onset of shear-coupling effects in off-axis tests,[13] hence acting as benchmarks for the off-axis experiments. In order to analyze the variability of the tensile data that was to be collected, ten CRE experiments were initially performed in the warp (0°) orientation. These CRE experiments are represented by test specimens AR-001 through AR-010, and the significant results of these tests, including yield strength, ultimate tensile strength, etc. are presented in Table 3. Values from experiments are normalized here to help emphasize variation, with $A_o = 0.00248$ in^2(1.60 mm^2), $k_o = 2327\,^{\text{lb}}/_{\text{in}}$ $(407.5\,^{\text{kN}}/_{\text{m}})$, $S_{yo} = 11.4$ksi(78.6MPa) $UTS_o = 12.7$ksi(87.6MPa), $S_{fo} = 11.9$ksi(82.0MPa), and $\epsilon_{fo} = 0.084$ in (2.13mm). Note that the cross-sectional area, A_o, represents the homogenized continuum assumption shown in Figure 1b. The highest degree of standard deviation observed in the normalized data was in the elongation to failure, with an acceptable value of 0.12. Yield strength and stiffness also show notable normalized standard deviations, with values of 0.04, and 0.10 respectively. These values are considered within statistical error limits for mechanical testing of this class of materials, and so it was justified to proceed with further testing of the material without multiple test duplications.

The mechanical response of the most representative warp (0°) sample (AR-003), and the weft (90°) sample (AR-016) are presented in Figure 5a. Points δ_A and δ_B, shown in the figure, are key points to be studied using FEM. It is clear that the weft (90°) orientation possesses superior strength and stiffness with respect to the warp (0°) orientation, and that it also undergoes more substantial work hardening. The failure characteristics of the two main orientations vary significantly, with the weft (90°) orientation failing abruptly and thoroughly upon reaching its ultimate tensile strength, and the warp (0°) orientation displaying more ductile behavior with a gradual unloading.

Analysis of the material in the weft (90°) orientation reveals some details about the nature of the mechanical response of woven materials in general. The material undergoes three stages of loading when placed in tension, as illustrated in Figure 5a. Stage 1 corresponds to tightening and potential sliding occurring between the adjacent and orthogonal wires, and is considered a non-linear and non-recoverable stage, as frictional forces would prevent the mesh from recovering sliding and tightening displacements. Stage 2 represents the elastic portion of the loading phase, during which wire deformation is dominated initially by crimp interchange, and subsequently by wire tensioning. Crimp interchange, studied in detail by Cavallaro and co-workers,[1] is the phenomenon in which the pre-crimped weft wires attempt to straighten, and in effect cause the warp wires to become crimped. Stage 3 represents the elastic-plastic transition, followed by the non-linear strain-hardening of the material.

The tensile response of the 325×2300 316 L stainless steel woven wire mesh varies significantly with orientation. Parameters such as stiffness, yield strength, ultimate strength, toughness, and elongation to rupture are all highly dependent on orientation. The orientation dependence of the mechanical response of the mesh when subject to displacement controlled tensile testing is provided in Figure 6. Maximum stiffness, yield strength, and ultimate strength are observed in the weft (90°) direction at 2.88 kip/in (504.0 kN/m), 23.0 ksi (158.6 MPa) and 34.4 ksi (237.2 MPa) respectively. Minimum yield strength occurs in the 45° orientation at 1.8 ksi (12.4 MPa); however, this orientation shows exceptional toughness of 2.35 ksi (16.2 MPa). Minimum ultimate strength is observed in the 30° orientation, with a value of 7.66 ksi (52.8 MPa). Stage 1

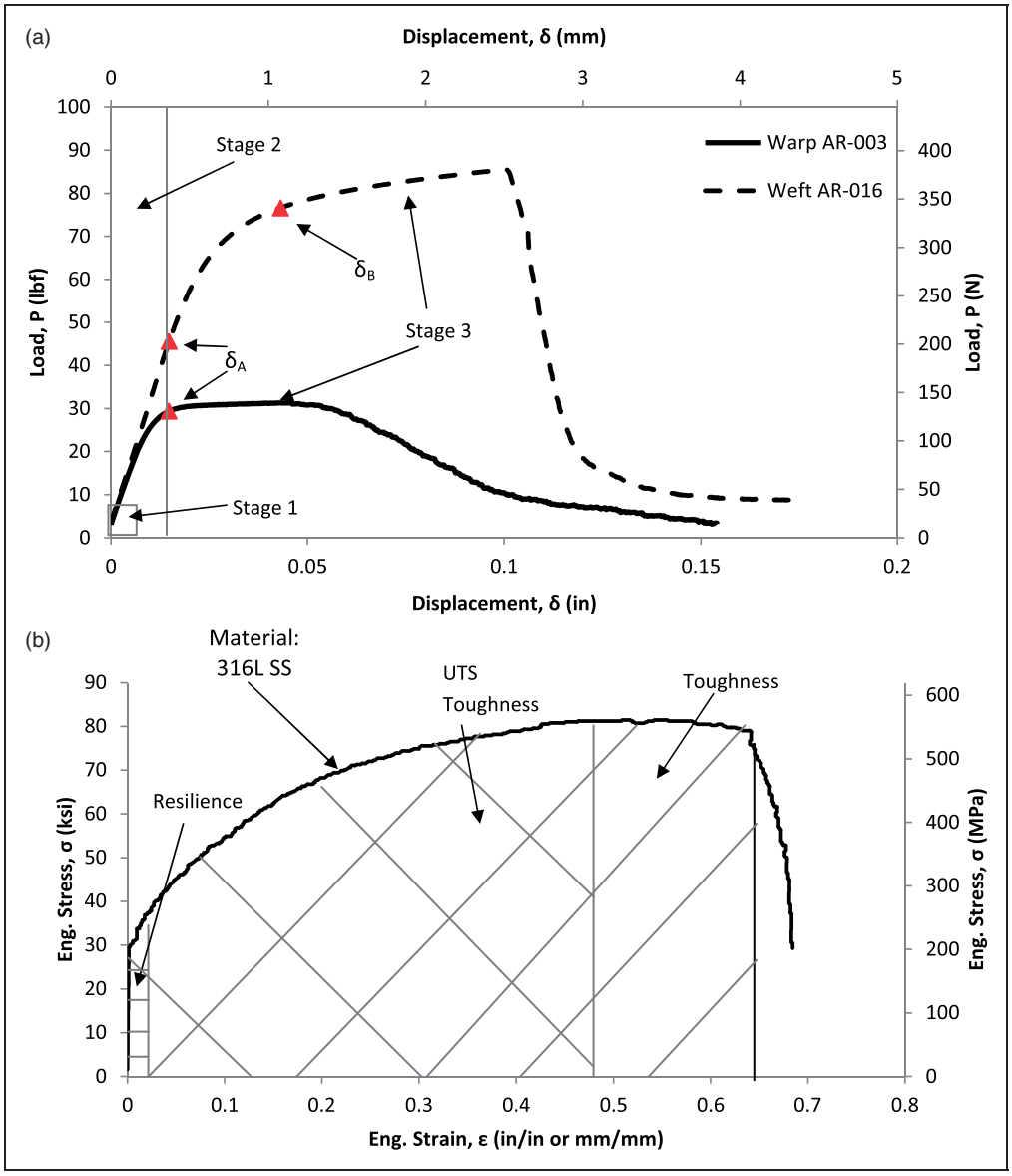

Figure 5. a) Mechanical response of main weave axes of 325 × 2300 316 L stainless steel woven wire mesh subject to constant rate extension tensile testing; b) typical stress-strain curve for 316 L SS[12] showing key toughness zones used to analyze the behavior of the woven wire mesh.

loading becomes more pronounced as the material orientation approaches 45°, where shearing effects cause the weft wires to rotate slightly on their contact points with the warp wires. Most orientations display predominantly linear behavior during stage 2 loading; however, the 30° and 60° orientations display distinctly nonlinear behavior. The warp (0°) direction displays a local maxima for yield strength and ultimate strength through 45°, but with significantly less toughness, 885.7 psi (6.11 MPa), than the weft (90°) direction. The warp (0°) orientation also shows the least elongation to fracture, and very little potential for work hardening. The 45° orientation shows the largest elongation to fracture, and undergoes a much larger amount of work hardening than any other orientation. Two orientations, 30° and 45°, show multiple yield points. The appearance of this phenomenon in multiple tests suggests that it is not an inconsistency in the data resulting from a poor test or end condition. The yield strength, stiffness, and elastic modulus reported for these orientations reflect the initial observed yield points. Table 4 provides normalized mechanical properties such as yield strength, ultimate tensile strength, stiffness, and elongation to failure of 325 × 2300

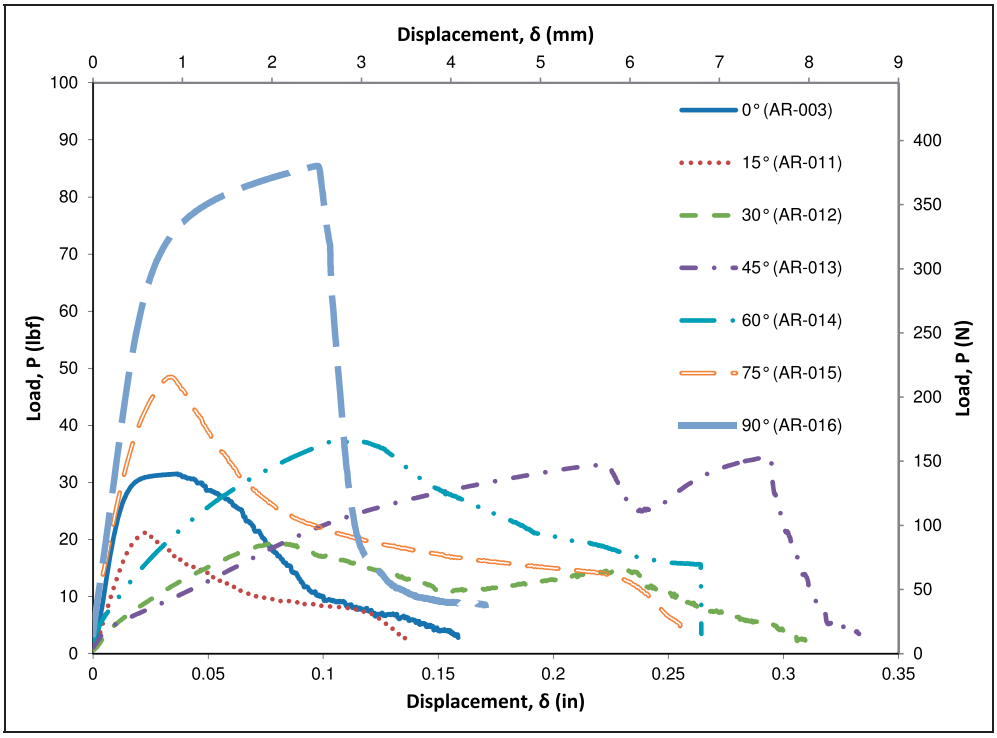

Figure 6. Orientation dependence of the mechanical response of 325 × 2300 316 L stainless steel woven wire mesh subject to constant rate extension tensile testing.

Table 4. Orientation dependence of normalized material properties of 316 L SS woven wire mesh

Specimen ID	Orientation, θ (deg)	Cross-Sectional Area, A/A_0	Stiffness, k/k_0	Yield Strength, S_y/S_{y0}	Ultimate Strength, UTS/UTS_o	Fracture Stress, S_f/S_{f0}	Elongation, $\in_f/\in_{f0}$
AR-011	15	1.00	0.56	0.66	0.67	0.68	0.98
AR-012	30	1.02	0.12	0.60	0.60	0.60	3.78
AR-013	45	1.02	0.24	0.16	1.07	0.92	4.55
AR-014	60	1.02	0.20	0.96	1.16	1.21	3.30
AR-015	75	1.01	0.82	1.39	1.52	1.27	1.26
AR-016	90	1.00	1.24	2.02	2.71	2.48	1.62

stainless steel woven wire mesh with respect to material orientation, where the normalization values are as in Table 3. The reported properties may be deduced directly from Figures 5 and 6 as macro-scale characteristics of the material.

More in-depth analyses of the material response are also performed, with properties such as resilience, toughness, and the unloading slope of each orientation being investigated. The unloading slope was analyzed as a measure of brittleness of the fracture, which indicates possible concentration of material evolution. The 60° orientation shows the highest resilience, while the 45° orientation shows the least. The weft (90°) direction shows the highest degree of toughness, with the lowest toughness occurring in the 15° orientation. The weft (90°) orientation shows the most brittle failure, with a very steep unloading slope, and the 30° orientation possesses the most gradual unloading. These normalized results are presented numerically for each orientation in Table 5, where $u_{ro} = 81.5$psi (0.562MPa), $u_{utso} = 396.2$psi (2.73MPa), $u_{fo} = 885.7$psi (6.11MPa), and $k_{uo} = 503.4^{\text{lb}}/_{\text{in}}$ (88.16^{kN}/m). The various toughness values reported here are defined by Figure 5b.

Homogenous orthotropic modeling

The mechanical response of a woven wire mesh at the meso-scale is multifaceted and complex, with factors

Table 5. Normalized toughness and unloading characteristics of 316 L SS woven wire mesh

Sample ID	Orientation, θ (°)	Resilience, u_r/u_{r0}	UTS toughness, u_{uts}/u_{uts0}	Toughness, u_f/u_{f0}	Unloading slope, k_u/k_{u0}
AR-003	0	1.00	1.00	1.00	−1.00
AR-011	15	0.73	0.242	0.554	−0.461
AR-012	30	2.81	0.808	1.33	−0.223
AR-013	45	0.11	3.77	2.66	−0.957
AR-014	60	4.29	2.34	2.31	−0.413
AR-015	75	2.24	0.923	2.04	−1.19
AR-016	90	3.54	5.59	3.05	−8.77

such as crimp interchange, wire sliding, wire binding, and wire tensioning all occurring simultaneously and dependently. Comprehensive mechanical analysis at the wire level quickly becomes unwieldy, and so an assumption that allows for the analysis of the material at the macro level is ideal. The assumption of homogeneity enables these materials to be modeled with a simplified orthotropic constitutive model; furthermore, taking advantage of mesh geometry allows the assumption that woven meshes behave as thin orthotropic sheets under plane stress, resulting in simple elastic constitutive equations,

$$\begin{bmatrix} \epsilon_x \\ \epsilon_y \\ \gamma_{xy} \end{bmatrix} = \begin{bmatrix} \frac{1}{E_x} & \frac{-v_{yx}}{E_y} & 0 \\ \frac{-v_{xy}}{E_x} & \frac{1}{E_y} & 0 \\ 0 & 0 & \frac{1}{G_{xy}} \end{bmatrix} = \begin{bmatrix} \sigma_x \\ \sigma_y \\ \tau_{xy} \end{bmatrix} \quad (2)$$

Here E_x and E_y are the elastic moduli in the x and y directions respectively, and G_{xy} is the shear modulus. Of the two Poisson's ratios, v_{xy} and v_{yx}, one is dependant due to symmetry of the compliance tensor. It has been demonstrated in the literature[10] that woven fabric materials can be successfully modeled as orthotropic bodies using well established material models. Several such models are exercised herein to illustrate the effectiveness of the homogenized orthotropic body assumption at capturing the orthotropic response of the woven wire mesh in question.

Elastic modeling

The elastic modulus of homogenous orthotropic materials is highly dependent on material orientation with the maxima occurring at the 0° and 90° orientations, and the minima occurring somewhere in-between. By transforming the constitutive equations for an orthotropic thin sheet, it can be shown[13] that the elastic modulus of such a material follows a trigonometric relationship, that is,

$$E_\theta = \left[\frac{1}{E_1}\cos^4\theta + \left(\frac{1}{G_{12}} - \frac{v_{12}}{E_1}\right)\sin^2\theta\,\cos^2\theta + \frac{1}{E^2}\sin^4\theta\right]^{-1} \quad (3)$$

Using G_{12} and v_{12} as curve-fitting parameters, equation 3 serves as an elastic model to illustrate that the woven wire mesh behaves as expected for an orthotropic sheet in the elastic domain. It is noted that equation 3 ignores the affects of shear coupling, and future work is planned to define the shear-coupling coefficient of the woven mesh to improve the validity of this model. Figure 7a illustrates the orientation dependence of the elastic modulus of the representative material, along with the distribution predicted by equation 3, referred to as the elastic modulus orientation function (EMOF). In its current form, equation 3 simply serves as a tool to illustrate that the elastic behavior of metallic woven structures can indeed be modeled using well established homogenous orthotropic relations, evidenced by the exceptional regression coefficients of 0.85 and 0.98 for the single and double wide data, respectively. Table 6 provides the values used in the EMOF to produce the curve fits for the elastic modulus. Here, E_1 and E_2 represent the warp (0°) and weft (90°) orientation elastic moduli, respectively; E_o represents the elastic moduli for the single wide warp (0°) used to normalize the data (1.28 Msi or 8.83 GPa); v_{12} represents the regression modeled Poisson's ratio; and G_{12} represents the modeled shear modulus.

Double wide specimens produced moduli values that are generally higher than their single wide equivalents. The 30° orientation double wide elastic modulus shows the maximum percent difference with the single wide at 98.4%. Variation in the off-axis double wide elastic moduli could potentially be attributed to the relatively small aspect ratio of the double wide samples. It has

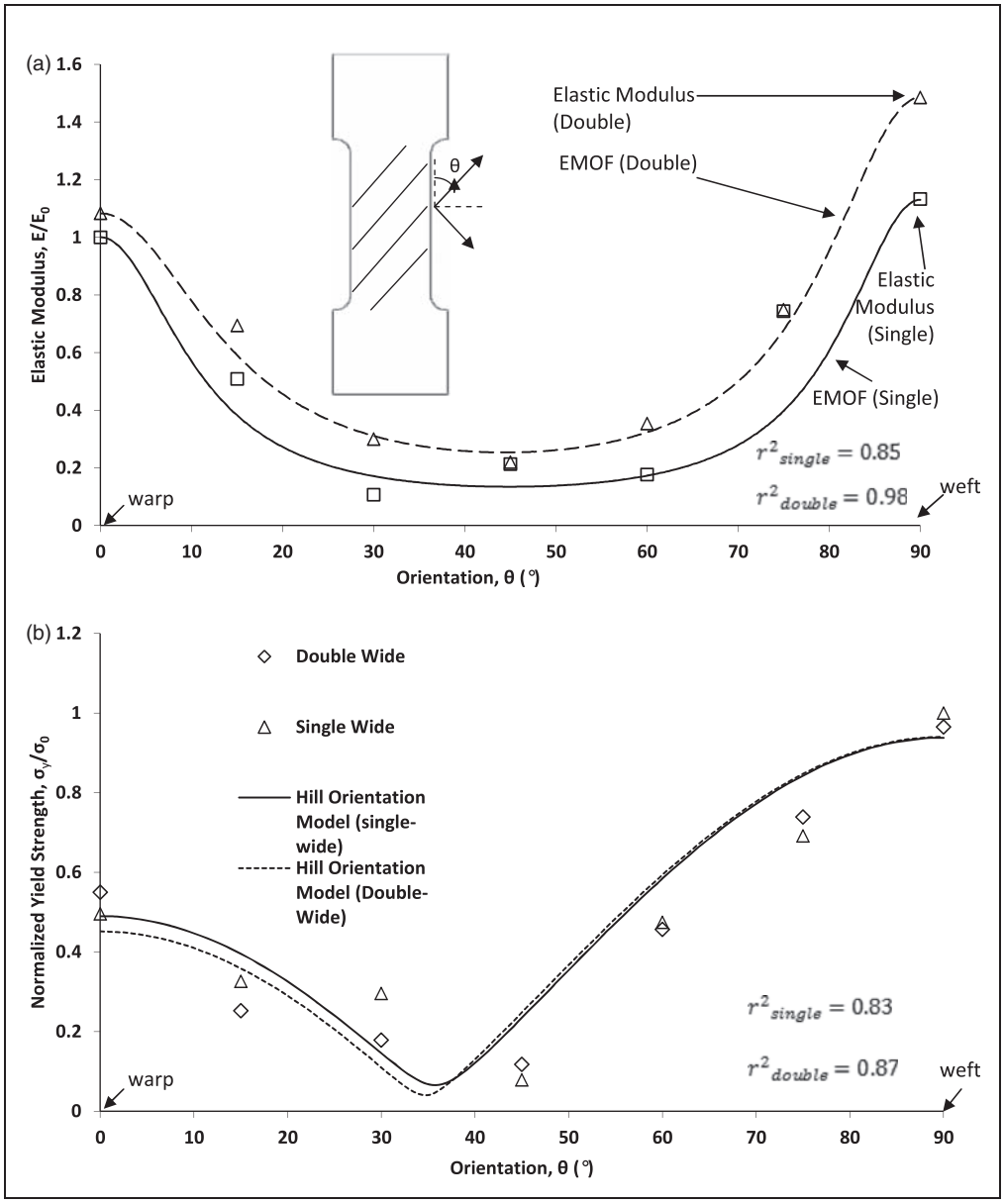

Figure 7. Orientation dependence of a) elastic modulus, and b) yield strength of 325 × 2300 316 L stainless steel woven wire mesh.

Table 6. Normalized constants from elastic modulus orientation function for 316 L SS woven wire mesh

	Warp elastic modulus, E_1/E_0	Weft elastic modulus, E_2/E_0	Poisson's ratio, ν_{12}	Shear modulus, G_{12}/E_0
Single wide	1.000	1.130	0.350	0.035
Double wide	1.083	1.485	0.350	0.068

been shown[14] that orthotropic specimens which exhibit shear coupling may be affected by adverse boundary conditions if clamped at both ends, as is the case in this study. Such clamped end conditions produce bending moments and shear forces that may distort the sample, creating a non-uniform stress distribution that impacts test results. Short and wide specimens are more adversely affected by these end conditions than

longer and narrower ones because the majority of the gauge length is not sufficiently removed from the boundary to mitigate the effects.[15] The degree to which the boundary conditions may affect the double wide off-axis modulus values is unclear, but it is noted that several of the orientations (0°, 45°, and 75°) produced results within error limits with respect to the single wide samples. Future work is planned to investigate the impact of shear coupling on the observed off-axis material properties for 316 L SS woven wire mesh.

Elasto-plastic modeling

Hill's failure criterion,[16] is widely used for anisotropic, orthotropic, and transversely-isotropic solids. The theory is based on Distortion Energy Theory, and can be shown to reduce in the case of isotropy. The criterion relates the overall yield strength of the material to the principal directions through the use of several curve-fitting parameters, resulting in a second order polynomial, for example

$$F(\sigma_y-\sigma_z)^2+G(\sigma_z-\sigma_x)^2+H(\sigma_x-\sigma_y)^2+2L\tau_{yz}^2+2M\tau_{zx}^2+2N\tau_{xy}^2=1 \quad (4)$$

The terms *F, G, H, N, M*, and *L* are determined experimentally through an orientation study of the tensile yield strength of the material. This relation may be reduced for the plane stress case, where only *F, G, H,* and *N* are needed. The necessary constants may be ascertained from a regression analysis with the yield strengths of the material in the principle orientations, and at several intermediate orientations.[13] In this way, the uniaxial experiments conducted at various orientations were used to develop the Hill parameters for the 316 L SS woven wire mesh.

The dependence of the normalized yield strength of the 316 L SS woven wire mesh on material orientation, with $\sigma_0 = 23.0$ ksi (158.6 MPa), is presented graphically in Figure 7b. The Hill analogy[16] was employed in an effort to model the orientation dependence of yield strength for the 316 L SS woven wire mesh. The yield criterion proved adequate as a model to formulate the failure (defined as global yielding) of the material with respect to orientation, yielding r^2 values of 0.83 and 0.87 when applied to the single and double wide data, respectively. Although the developed model does not take into account the formulation of wire damage, nor the mode of wire failure, this model does allow for very useful macro-level strength predictions. It is noted that Hill's analogy, in the form presented here, does not account for the shear coupling exhibited by this material, which is believed to be the cause of the observed 'waviness' in the orientation dependence of the experimental yield strength. The future addition of shear-coupling terms to Hill's analogy is planned in an effort to improve the model. The optimal single and double wide Hill orientation models for the 316 L SS woven wire mesh are presented in Figure 7b, along with the normalized yield strengths. It is noted that the orientation model predicts minimum yield strength at about the 35° orientation, whereas experiments have shown minimum yield strength in the 45° orientation. The optimal Hill analogy parameters for the representative material are provided in Table 7. The similarity of the two Hill analogy curves (single and double wide) provides strong evidence that the double wide specimens are sufficiently wide to capture the behavior of the material, and that further specimen widening will not appreciably affect the test results.

Table 7. Experimentally determined Hill's Analogy parameters for 316 L SS woven wire mesh

Parameter	G [1/ksi^2] or [1/MPa^2]	F [1/ksi^2] or [1/MPa^2]	N [1/ksi^2] or [1/MPa^2]	H [1/ksi^2] or [1/MPa^2]
Single wide	0.770	1.410	−0.980	−0.530
Double wide	0.550	1.230	−0.767	−0.346

The percent difference of single and double wide yield strengths is much higher in the warp dominant orientations than in the weft dominant orientations. The double wide yield strength observed in the warp (0°) orientation is within 10% of the mean single wide warp (0°) yield strength. It has been previously shown that single wide warp (0°) samples (AR-001 through AR-010) display a considerable amount of variation in their yield strengths, and so significant double wide strength variation in the warp dominant orientations (i.e., 0° through 30°) is not unfounded. Strength variability may be explained by the unloading behavior observed in these orientations. The gradual unloading slope observed in the warp (0°) orientation, shown in Figure 5a and quantified in Table 5, implies a dispersed fracture process zone, leading to inconsistent yielding of the woven wire mesh in warp dominant orientations. As the orientation moves beyond 45° and becomes weft dominate, the degree of scattering goes from a maximum of 49.5% at 30°, to less than 5% at 90°; considered well within statistical error limits for this type of testing.

Voce hardening model

In order to aid in the classification of the elasto-plastic behavior of 316 L SS woven wire mesh, the strain

Table 8. Voce hardening model parameters for SS 316 L woven wire mesh (single wide)

Orientation, θ (°)	Stiffness coefficient, R_0 [lbf] or [N]	Hardening coefficient, R_∞ [lbf] or [N]	Hardening exponent, b
0	9.00	10.0	290
15	10.0	4.00	180
30	20.0	2.20	135
45	238	1.00	1000
60	242	1.00	220
75	550	3.30	250
90	145	15.0	120

hardening behavior of the material at each orientation was modeled via a Voce hardening relationship,

$$P_h = P_y + R_0\left(\frac{\delta_p}{L_0}\right) + R_\infty\left[1 - e^{-b\left(\frac{\delta_p}{L_0}\right)}\right] \qquad (5)$$

The current formulation is a slightly modified version from the original model.[11] Rather than stress versus plastic strain, load versus plastic displacement is modeled. The model contains three parameters that are determined through inspection of the tensile test results. For example, R_∞, the strain hardening coefficient, is the difference between the proportional limit and yield strength of the respective material. In addition, R_0, the stiffness coefficient, controls the hardening rate, and b, the strain hardening exponent, influences the elasto-plastic transition curvature. In addition to these terms, P_y, is the observed proportional limit, L_0, is the specimen gauge length, P_h is the modeled plastic load, and δ_p is the plastic deformation. Regression analysis was performed to develop the optimal parameter value for each orientation, and these hardening parameters are provided in Table 8. The modified Voce hardening model plots are provided in Figure 8 in conjunction with the single wide tensile test results in the elasto-plastic region. The Voce model proves very capable of describing the hardening behavior through the ultimate tensile strength for this class of material, particularly at the main material orientations, as evidenced by the r^2 values reported in the figure, all of which are measured up to P_{uts}, the observed ultimate tensile load.

Orientation effects on mesh failure

The characteristics of the observed failure surfaces for the CRE-tested woven wire mesh single wide specimens were studied in an effort to gain insight into the failure mechanisms and local fracture evolution. Qualitative and quantitative observation of failure surfaces have been made by previous authors for this class of material,[10,17] and it has been shown to provide insight into wire and mesh behavior. This investigation revealed a strong dependence of fracture orientation and appearance on material orientation. Observations were made from detailed inspection of the failure surfaces, post fracture, for each material orientation tested, with focus on the degree of wire pull-out (fraying), number of fractures, waviness of the fracture surfaces, orientation of the fracture with respect to loading, and the direction of fracture propagation. The failure surface of each orientation in both wide and close views, along with respective fracture angles, θ_s, with respect to the loading axis is shown in Figure 9.

The warp (0°) orientation fractured with a considerable degree of fraying and fracture surface waviness. Failure occurs in the warp wires only, with very little if any load being transferred to the weft. As the warp wires deform and eventually fail, frictional forces between the warp wires and the orthogonal weft wires force the weft wires to 'pull-out' of the weave, causing the observed fraying. This orientation produced several areas of fracture, all of them with considerable waviness and distribution. This indicates that the evolution of plasticity is well distributed within the warp wires of the mesh, and that failure on the macro level may be considered independent of position in the warp direction. The initial observed fracture began at the edge of the sample and progressed inward as adjacent warp wires failed and unloaded, forcing neighboring wires to accept more load. Ultimately, a uniform strain evolution in the warp wires allows for a relatively slow unloading of the material, with failure occurring in the warp wires, and evolving orthogonal to the loading direction.

Failure in the weft (90°) orientation is much more concentrated than the warp (0°) case. No wire fraying is observed, and fracture propagates through the material quickly and in a straight path. Fracture occurred completely and instantly in two locations on the sample, both with identical features. The appearance of this failure surface indicates that the material evolved uniformly, but in a concentrated location of wire contact. Again, the failure surface is orthogonal to the loading direction, and the fracture initiates at the edge of the sample.

Intermediate orientations show combinations of the failure characteristics associated with the warp (0°) and the weft (90°). Shear coupling of the off-axis specimens leads to the formation of shear stresses in the uniaxially loaded samples,[13] and indication of this can be observed from the high degree of weft wire fray in 30°, 45°, and 60° samples. This phenomenon also

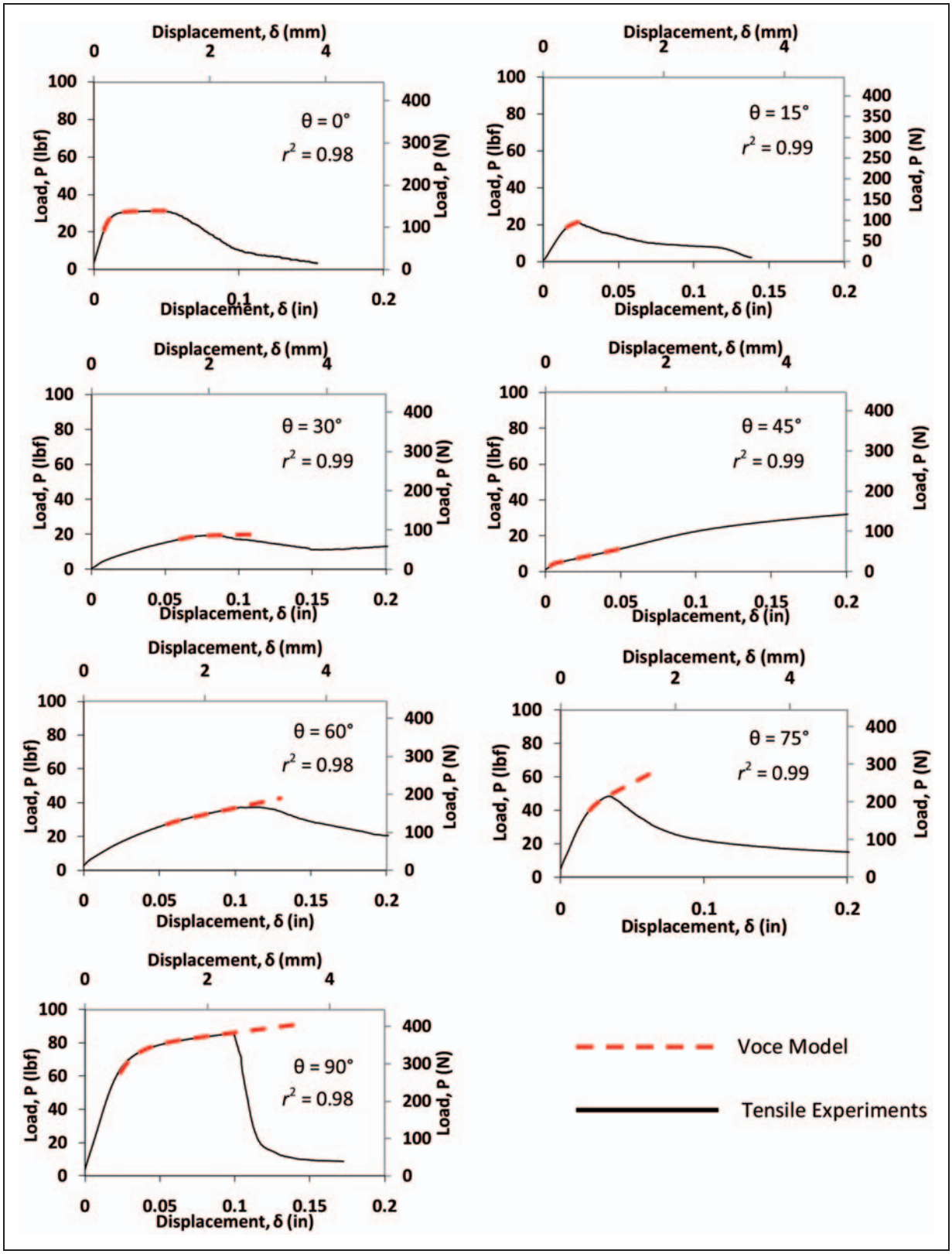

Figure 8. Modified Voce hardening models applied to 316 L SS woven wire mesh specimens at various orientations, with r^2 values through ultimate tensile strength.

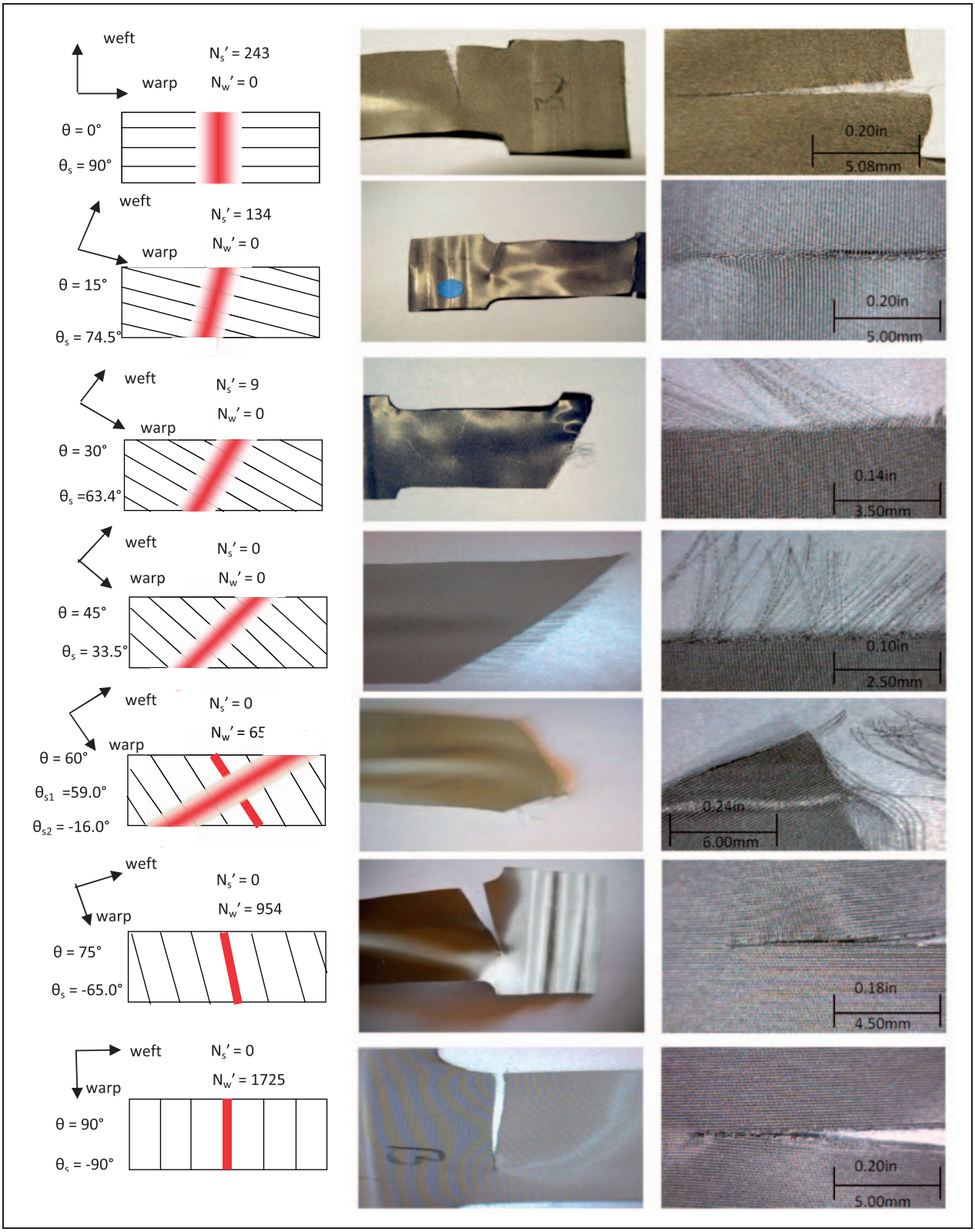

Figure 9. Fracture images of single wide 316 L SS woven wire mesh at various orientations.

produces a small degree of sample waviness attributed to shear forces that cause the wires to rotate slightly about their contact points. Also observed was a tendency for the failure orientation to differ somewhat from the orthogonal orientations found in the warp and weft. The 60° orientation marks a clear transition in the dominant mesh behavior, showing two distinct failure planes, each indicative of either a warp or a weft dominant wire failure. It is noted that the observed transition to weft dominant failure characteristics at the 60° orientation is supported by equation 1, which calls for the weft wires to become active in the loading at 59.1°. The exact point of transition is of great interest to future study, and may serve as a benchmark for users of this material to develop the optimum material orientation for their respective application. Multiple but identical failure surfaces formed in the 15° and 75° orientations, each with two fractures on opposite ends of the sample. The remaining off-axis orientation displayed only one failure surface.

Damage evolution

Ratcheting experiments

Ratcheting experiments on the double wide test specimens provide high resolution data regarding the change in stiffness of the material as it was loaded and unloaded in a series of several ratcheting cycles. The tests produced load-displacement data for each cycle, shown in Figure 10. The ratcheting cycle displacement rate was controlled for both loading and unloading phases in an effort to mitigate any rate dependant effects on the mechanical response,

$$\delta(t) = 0.00032t + \left[\frac{0.012}{a}\left[(t+7) - a\left[\frac{(t+7)}{a} + \frac{1}{2}\right]\right](-1)^{\left[\frac{(t+7)}{a} - \frac{1}{2}\right]}\right] + 0.005 \quad (6)$$

Here, $\delta(t)$ represents a mathematical model of the applied ratcheting cycle, where $a = 7.75$ represents half of one period, t is measured in seconds, and δ is provided in inches.

Upon investigation of the double wide ratcheting test results, it is evident that hysteresis loops develop during each ratcheting cycle. Hysteresis present in the elastic region ratcheting cycles indicate energy losses in the material not attributable to plasticity, providing some insight into the degree of non-recoverable wire sliding and frictional rubbing that occurs in stage 1 loading. In order to quantify the energy losses present in these loops, trapezoidal integration was performed at load cycles before yield, at half of the ultimate strength, and at the ultimate tensile strength for warp (0°), weft (90°), and 45° orientations, for example

$$E_h = \int_a^b L(\delta)_{\delta:\, a\to b} - L(\delta)_{\delta:\, b\to a} \mathrm{d}\delta \quad (7)$$

Here, E_h is the hysteresis energy, and $L(\delta)$ is the load versus displacement response over a ratcheting cycle from point a to point b as indicated on Figure 11b. As shown in Figure 11, maximum hysteresis energies were observed in initial cycles of each orientation, with the weft (90°) having the largest energy at 4.4×10^{-3} ft-lb (5.9×10^{-3} J). Little difference was observed between the initial hysteresis energies of the 45° and the warp (0°) orientation, each with losses of 9.1×10^{-3} ft-lb (1.2×10^{-3} J). In general, as the material evolves in each orientation, frictional hysteresis is replaced by plasticity, and the observed hysteresis energy decreases. Minimum values occurred at the ultimate strength for each orientation, again with the weft (90°) displaying the largest energy loss of 2.2×10^{-3} ft-lb (2.9×10^{-3} J). The 45° orientation possessed a hysteresis energy of 2.5×10^{-4} ft-lb (3.3×10^{-4} J), while the warp (0°) orientation remained more constant, displaying an energy loss of 7.5×10^{-4} ft-lb (1.0×10^{-3} J). These results indicate that the energy lost during elastic loading is significantly higher in the weft (90°) direction of this material than in the warp (0°) direction (131.25% difference at the initial stage), illustrating how the degree of frictional wire interaction varies between the main weave orientations.

Continuum damage model

The use of ratcheting type tensile tests on the double wide samples allowed for the formulation of a damage model for the 325×2300 316 L SS woven wire mesh based on the degradation of its elastic modulus. The accumulation of damage can be observed as degradation of the stiffness of the wire mesh as it is subjected to increased strain in each successive ratcheting cycle, ultimately ending in the failure of the specimen. The evolution of the elastic modulus of the woven mesh throughout the ratcheting experiments in each orientation is shown in Figure 12. A damage model was sought in an effort to eventually develop a failure criterion for the 325×2300 316 L SS woven wire mesh based on continuum damage mechanics (CDM). Such a model has been developed based on the fundamental isotopic damage theory, which requires the introduction of a damage variable, D, defined by

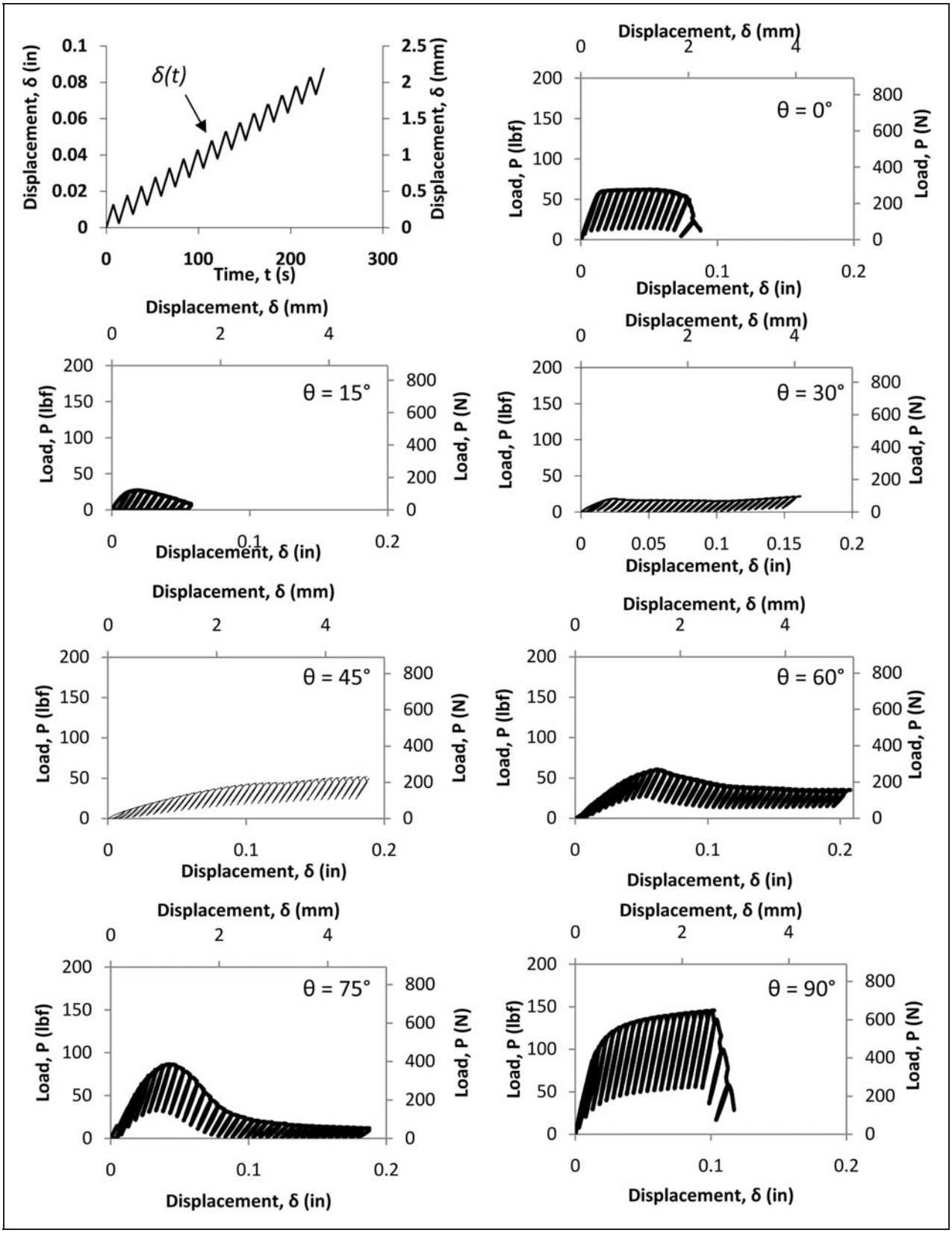

Figure 10. Mechanical response of 325 × 2300 316 L SS woven wire mesh under ratcheting type tensile testing at various orientations.

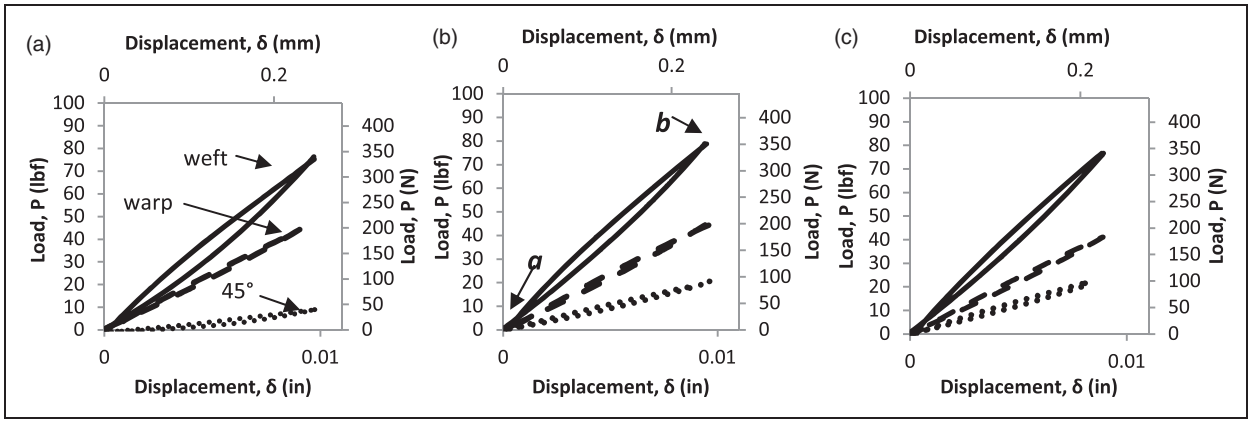

Figure 11. Hysteresis loops of 316 L SS woven wire mesh at various orientations; a) initial cycle, b) half of UTS cycle, c) UTS cycle.

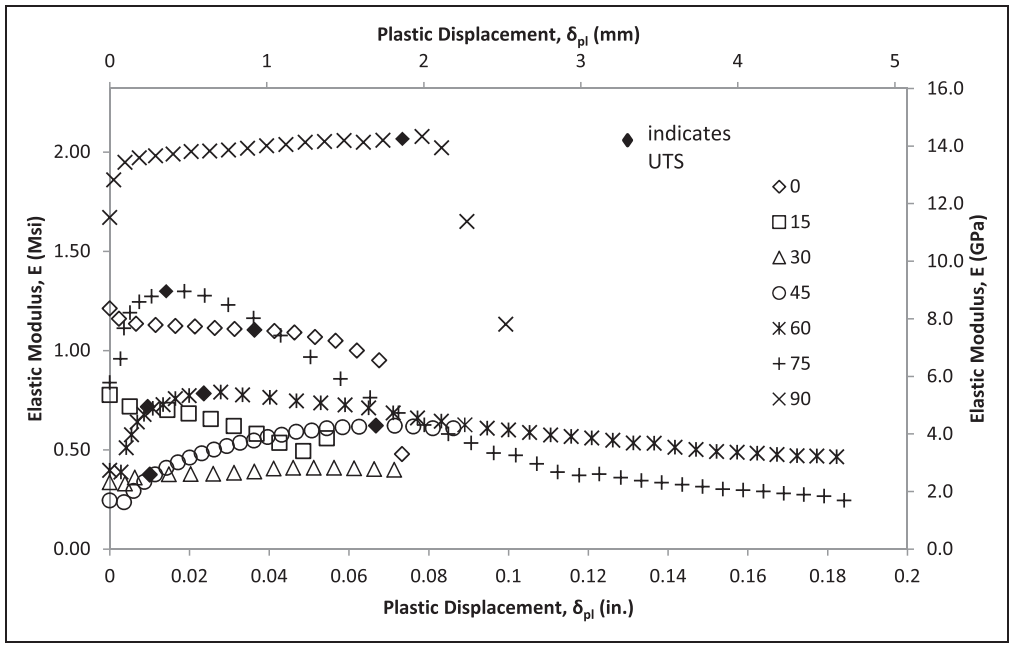

Figure 12. Evolution of the elastic modulus of double wide 325 × 2300 316 L woven wire mesh subject to ratcheting tensile testing at various orientations.

the change in elastic modulus after plastic deformation by

$$D_\theta = 1 - \frac{E_{D\theta}}{E'_\theta} \tag{8}$$

Here, $E_{D\theta}$ is defined as the damaged elastic modulus for each respective orientation and E'_θ is the initial elastic modulus for each respective orientation. The independent treatment of each orientation simplifies the damage modeling by alleviating the need for an orthotropic model, and so only the elastic modulus in the orientation in question need be considered. The damaged modulus, $E_{D\theta}$, was modeled for each orientation via a curve fit to the experimental data producing a function dependent on the plastic displacement, $\delta_{pl}(t)$, the observed undamaged elastic modulus, E'_θ, and several curve-fitting parameters, for example.

$$E_{D\theta} = E'_\theta - \frac{m}{e^{c\delta pl(t)}}\delta_{pl}(t) + E_m\left[1 - e^{-b\delta_{pl}(t)}\right] \tag{9}$$

To provide consistency and synergy to this relationship, the damage formulation was designed after equation 5 and the Voce model. Here, E_m the modulus coefficient, represents the difference in elastic moduli from the initial value, E'_θ, to the first inflection point

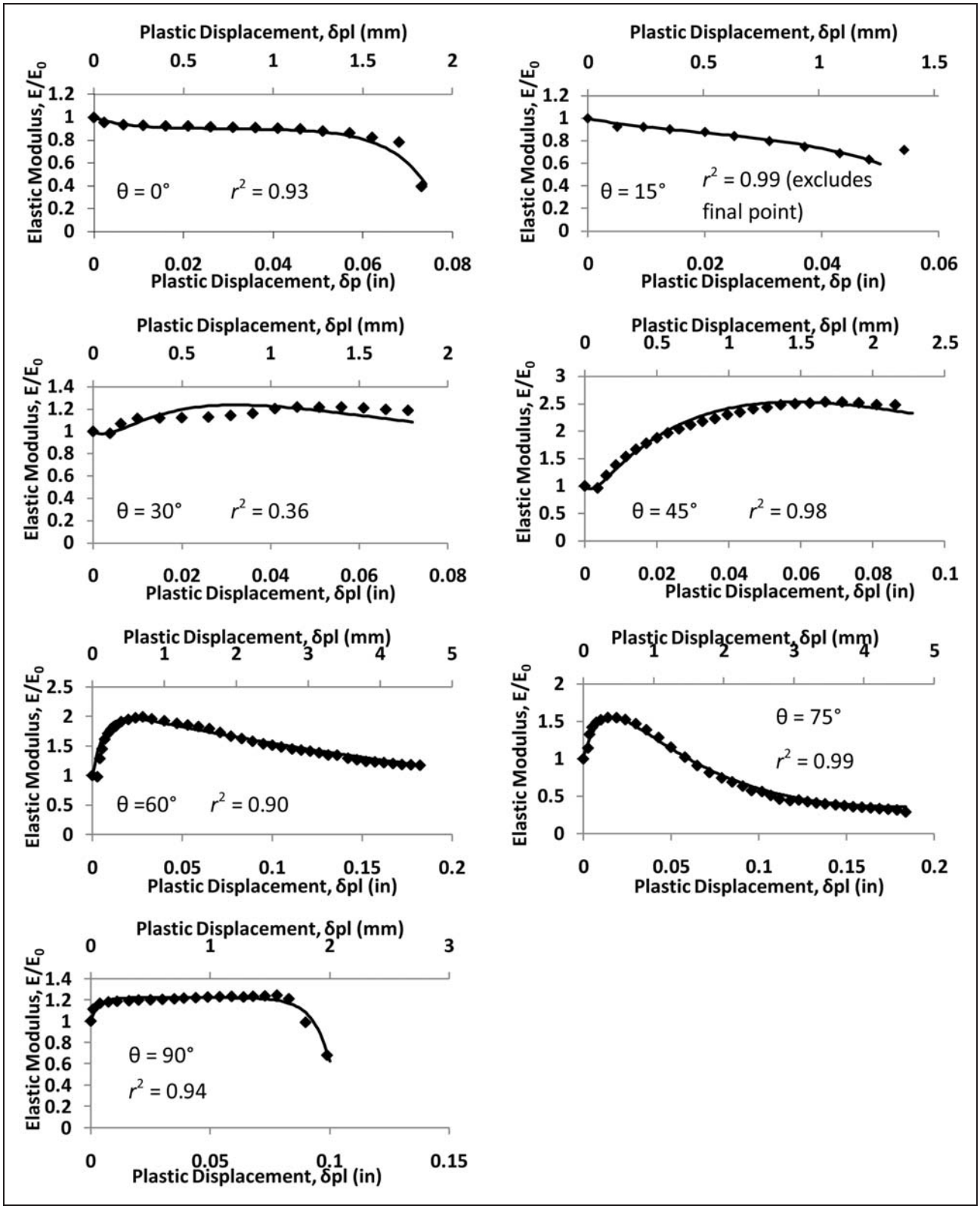

Figure 13. Actual and correlated elastic modulus evolution for 325 × 2300 316 L SS woven wire mesh at various orientations.

Table 9. Elastic modulus degradation model parameters for 316 L woven wire mesh

Orientation, θ (°)	Slope coefficient, m	Modulus coefficient, E_m [ksi] or [MPa]	Modulus exponent, b [1/in] or [1/mm]	Slope exponent, c [1/in] or [1/mm]
0	0.003	−0.100	150	−104
15	1.00	−0.100	100	−36.0
30	−36.0	−0.200	225	29.5
45	−88.0	−0.350	500	17.2
60	7.00	1.150	160	1.50
75	28.0	1.200	100	5.60
90	0.00001	0.220	300	−133

of the model. Also, m and c, the slope coefficient and exponent respectively, are curve-fitting parameters that control the rate of elastic moduli change after the first inflection point, while b, the modulus exponent, influences the initial curvature of the model. For ease of use, equation 9 was fitted to data normalized by the initial elastic modulus for each respective orientation, such that $E'_\theta = 1$ for every orientation. As shown in Figure 13, this model proves quite capable of capturing the gamut of behaviors of the elastic modulus of this material throughout its entire evolution, and when using the parameter values given in Table 9, provides good damage results when compared to experimental data. Investigation of the elastic moduli trends shown in Figures 12 and 13 reveal an unusual increase in elastic moduli through ratcheting cycles for several weft dominant orientations. This indicates a significant amount of material stiffening, particularly in the 45°, 60°, and 75° orientations. This behavior produces negative damage values when equation 9 is employed in its current form, but it is noted that the conventional definition of damage is satisfied with this method. Use of this model is currently limited to uniaxial loading cases, as well as to the prescribed displacement function, but future work is aimed at expanding this damage model to include general plane orthotropic loading.

Finite element analysis

The use of the finite element method to study this class of materials is ideal in that it gives the ability to correlate the meso-scale stress or strain distributions to the macro-scale behavior of the woven mesh. Numerical simulations were conducted using 3D finite elements with full contact definitions in order to obtain the highest amount of accuracy and resolution possible. While painstaking in practice, the definition of realistic frictional contact elements to handle the wire contact rather than idealized node to node springs or rigid elements provides for a fully functioning model capable of handling any combination of in-plane loading.

Model development

The woven wire mesh was modeled using ANSYS multi-physics FEM software. The rendering used to generate the finite element mesh is shown in Figure 1a. With the model satisfactorily defined, the geometry was meshed using ANSYS Workbench, which provided a sufficiently sophisticated GUI based FEM environment to carry out the simulations. The simulations were performed in a number of steps, first arriving at an optimal mesh that aided both convergence and stress distribution continuity. The mesh consisted of 20 node hexahedron elements (SOLID186), as well as sufficient 3D contact elements (TARGE170 and CONTA175). The overall node count was 28,769. An augmented Lagrange contact formulation was utilized to help stabilize the contact model, with adjustments being made to the contact stiffness to aid in convergence. The contact parameters used in the model included a static friction coefficient, contact stiffness factor, and a scoping region used to determine if contact was taking place (pinball region). Two different contact definitions were utilized; one to define warp to weft wire contact, and the other to define weft to weft wire contact. Weft to weft contact was assumed to have more relative wire sliding than normal force, and so required a small contact stiffness factor and friction coefficient to obtain convergence, with values of 0.01 and 0.02, respectively. Warp to weft contact was defined with a stiffness coefficient of 0.70, and a more realistic friction coefficient of 0.50. ANSYS was allowed to automatically determine the optimal pinball region for the contact, and was allowed to turn symmetrical contact regions off in an effort to reduce contact chatter and aid convergence. Reduction in contact stiffness results in the need to increase the stiffness of the constitutive matrix employed by the numerical model. The resulting

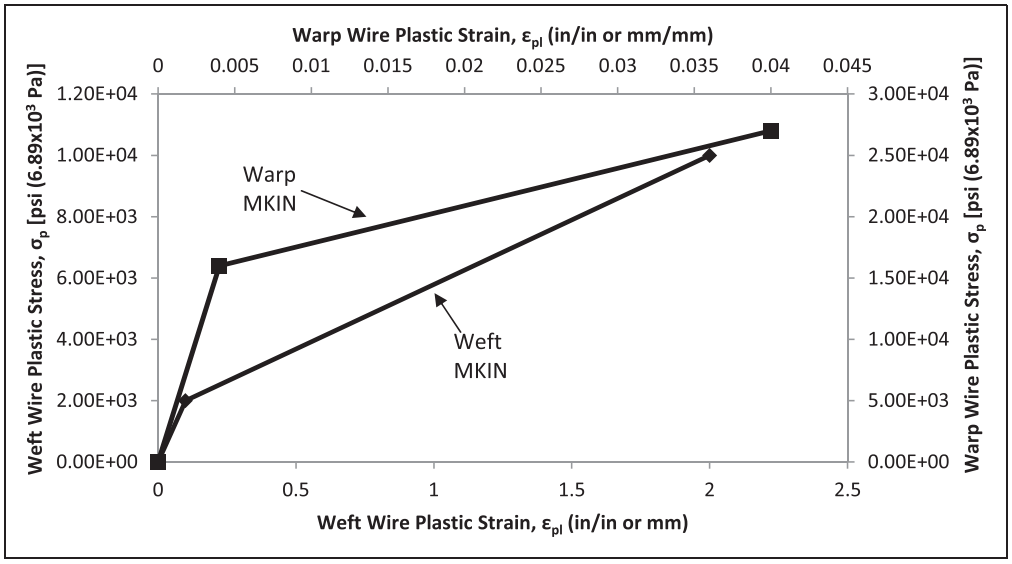

Figure 14. Multi-linear kinematic hardening models used to simulate the hardening behavior of the warp wires and the weft wires for the 316 L SS woven wire mesh.

Table 10. Material properties of warp and weft wires as defined in FEM constitutive model

Property	Elastic modulus, E	Yield strength, S_y	Ultimate tensile strength, UTS	Density, ρ	Poisson's ratio, ν
Warp					
SI	51.7 GPa	400 MPa	586 MPa	0.008 g/mm^3	0.3
English	7.5 Msi	58.0 ksi	85.0 ksi	0.289 lbf/in^3	0.3
Weft					
SI	448 GPa	1720 MPa	1709 MPa	0.008 g/mm^3	0.3
English	65 Msi	250 ksi	260 ksi	0.289 lbf/in^3	0.3

multi-linear kinematic hardening (MKIN) model used for each wire (warp and weft) is therefore not indicative of the actual wire properties, but is instead tailored to match the CRE tensile test results from warp (0°) and weft (90°) orientations. Figure 14 illustrates the plastic strain hardening response employed in the FEM for the 316 L stainless steel woven wire mesh. The material properties given to each wire in the model are provided in Table 10. Note the difference between the warp and weft material properties used in the model, with the weft wires being given far more strength and stiffness to fit the CRE test results, as well as differences between model properties and the published properties for 316 L SS in Table 2.

Boundary conditions

With the intent of the simulations being to mimic the tensile testing to the highest degree possible, a set of boundary conditions were generated to handle both 0° and 90° simulations, in which no shear displacement components were present. Loading was applied to the FEM via incremental linear displacements, much like the CRE tensile experiments. The magnitude of the applied displacements, and the model results, are related to the experimental samples via simple geometric relationships, such as

$$F_c = F_{sim}\left(\frac{W_{\exp}}{W_{sim}}\right) \tag{10}$$

$$D_c = D_{sim}\left(\frac{L_{\exp}}{L_{sim}}\right) \tag{11}$$

Each relationship is used to scale simulation results to the experimental results, where F_c and D_c are the scaled simulation force and displacement, F_{sim} and D_{sim} are the force and displacement from the model, L_{sim} is the length of the model in the loading direction, W_{sim} is the width of the model orthogonal to the

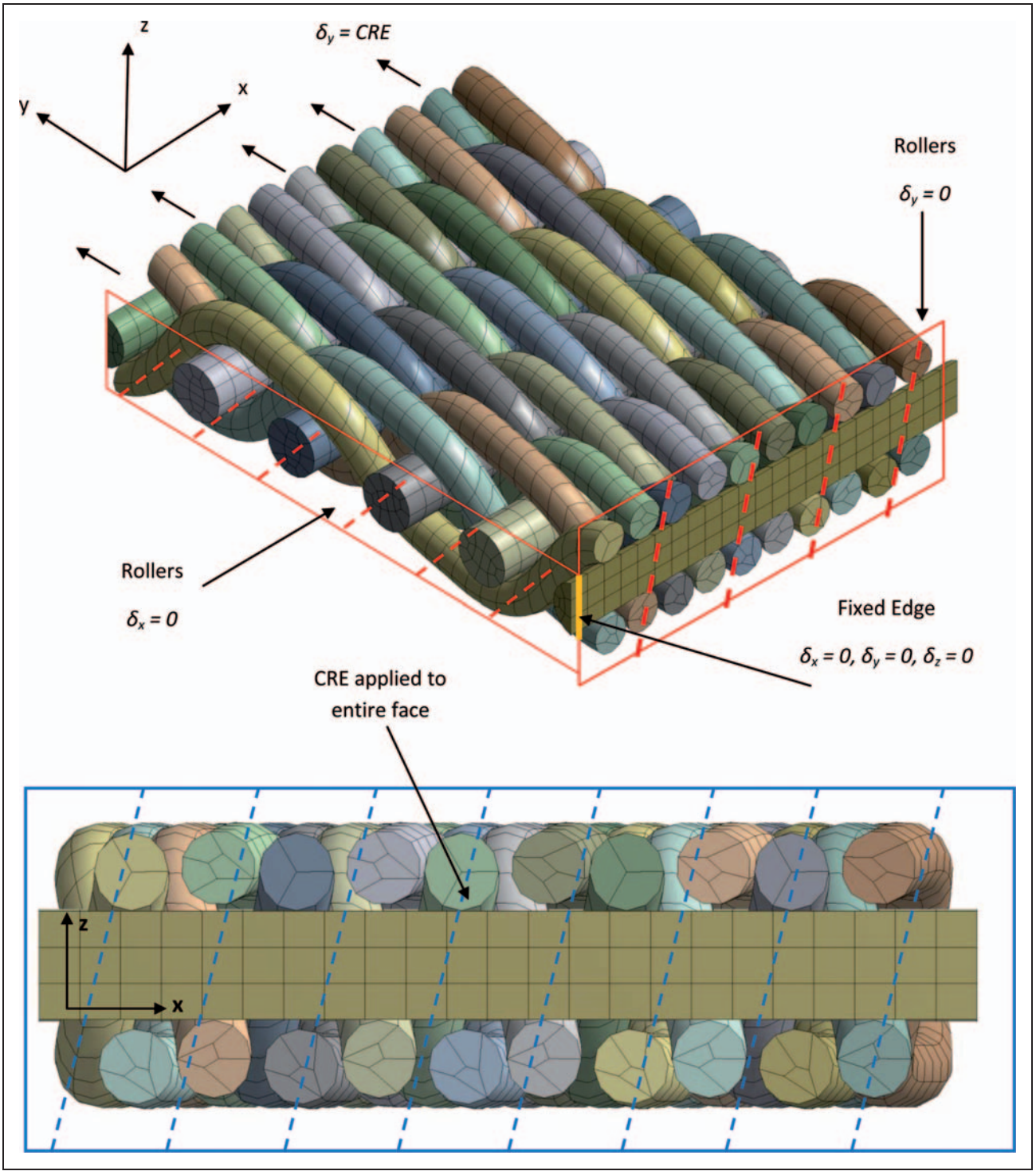

Figure 15. Finite element mesh of 3D CAD model used to facilitate the numerical modeling of the 316 L SS woven wire mesh with boundary conditions used to simulate the tensile testing of the weft (90°) orientation sketched.

loading direction, and L_{exp} and W_{exp} correspond to the gauge length and width of the test specimens, respectively. The use of displacements helps to ensure model stability, and that the simulations results are easily comparable to the experimental results. Figure 15 shows the boundary conditions applied to the model in the weft (90°) orientation, and by rotating the geometry 90°, the boundary conditions utilized on the warp (0°) direction simulations can be ascertained. Note that the frictionless supports act as symmetry constraints,

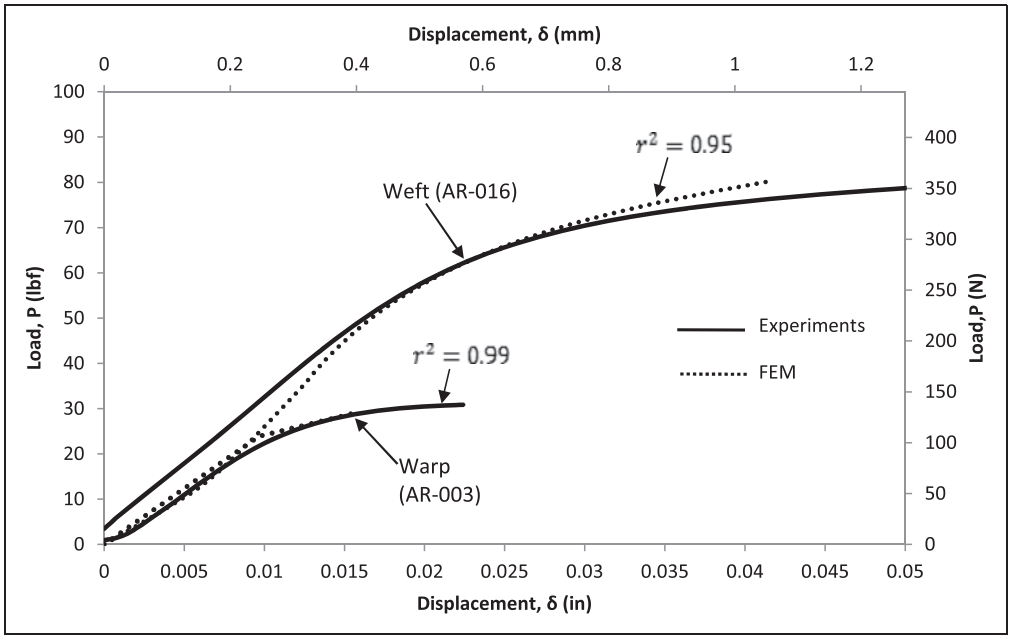

Figure 16. The elastic-plastic response of the Finite Element Model as compared to the mechanical response of the 325 × 2300 316 L stainless steel woven wire mesh subject to tensile testing in the warp (0°) and weft (90°) orientations.

and allow for full realization of Poisson's effect and wire tightening at the end locations, providing a realistic material response.

FEM results

Modeling efforts thus far have been focused on uniaxial tension in the main material orientations. Figure 16 shows the results of the main axes simulations with respect to the CRE tensile tests. Error in stiffness and yield strength of the simulation results is less than 10% with respect to the single wide experiments. The greatest load prediction error occurs in the weft (90°) orientation in the linear-elastic region at 18%; however, the critical elasto-plastic region shows an error of less than 5%. These results validate the mechanical model used to simulate the woven wire mesh, and justify the use of contour plots to study meso-level material behavior. These efforts reveal that much of the load is indeed carried by the warp wires, even in the case of loading perpendicular to their running length, indicating that crimp interchange is a significant pathway for strain distribution throughout the wire mesh structure. Contour plots of the plastic strain evolution of the main axes (warp and weft) are provided in Figure 17. These plots represent meso-scale plastic strains accumulated at key macro-level displacements, δ_A and δ_B, as indicated on Figure 5a, effectively relating macro mesh behavior to meso wire behavior in the elasto-plastic region. Average plastic strain accumulation at these points is 0.0016 in/in (or mm/mm) for the warp (0°) orientation and 0.0021 in/in (or mm/mm) for the weft (90°) orientation at $\delta_A = 0.015$ in (0.381 mm). At $\delta_B = 0.04$ in (1.016 mm), the average plastic strain accumulation is 0.044 in/in (or mm/mm) in the weft (90°) orientation. These values are taken from centralized nodes of the mesh in order to mitigate boundary condition effects on the results. Plastic strain in the weft (90°) orientation tends to accumulate at the area of warp-weft contact, indicating that failure should occur along the warp wire orientation as observed in the experiments. The accumulation of plastic strain in the weft orientation also explains the uniform brittle-like failure that occurs immediately after ultimate tensile strength was achieved. The warp (0°) orientation develops strain in a much more uniform manner, distributed evenly over the warp wires only. Strain propagates as one would expect in an homogenous body, with little gradient observed. This strain distribution also supports the gradual unloading observed for this orientation in CRE tests. Future modeling efforts are intended to expand the loading to general plane stress, including pure shear and biaxial tension conditions.

Conclusions

Extensive mechanical testing and material modeling has been carried out on a 325 × 2300 316 L SS twill-dutch woven wire mesh. Uniaxial tensile tests have been performed at various material orientations providing high

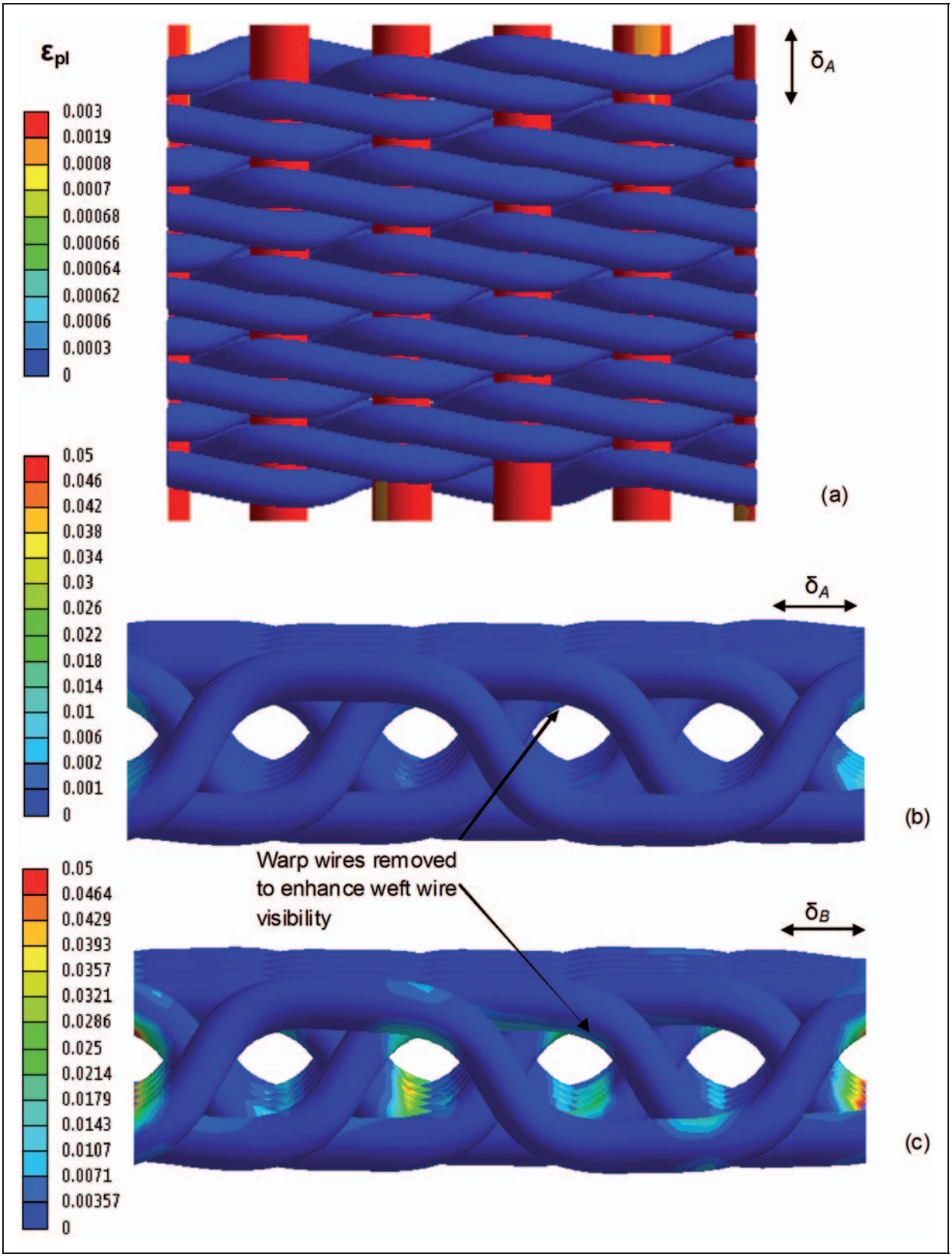

Figure 17. Equivalent plastic strain FEM contours of the 325 × 2300 316 L SS woven wire mesh subject to tensile loading in the a) warp (0°) directions; b) and c) weft (90°) direction.

resolution data and a good understanding of the orthotropic material behavior of this material. In an effort to justify the macro-scale modeling of this material, several classic models have been exercised with respect to the as-received (AR) mechanical data. Elastic, elasto-plastic, and hardening models have been applied to the material with excellent results. The orientation dependence of the elastic modulus has been shown to behave as expected for homogenous orthotropic materials. It has also been demonstrated that Hill's Analogy provides a reasonable model for the prediction of mesh yielding, and that the Voce hardening model provides excellent fit to the experimental results. These results suggest that classic macro-scale orthotropic modeling is sufficient to provide the designer with acceptable predictions of material behavior.

In an effort to investigate the macro-scale damage accumulation for this material subject to cycles of plastic deformation, a cumulative damage model was developed. Orientation dependant ratcheting type tensile tests were performed, and the progression of the material's elastic modulus through rupture was analyzed and modeled. The macro-scale damage model proved very capable of predicting the degradation in elastic modulus through rupture of this woven wire mesh material.

To further justify the use of macro-scale modeling to predict the behavior of this class of materials, a meso-scale FEM was developed. This model incorporated wire scale representation of the woven mesh, with several weave periods included to help mitigate boundary effects. The response of the model in the main material orientations has been shown to closely follow the macro-scale response, indicating that wire scale behavior need not be considered when making macro-scale design considerations. The distribution of plastic strain was also studied via the FEM, and it is demonstrated that the macro-scale mesh fracture behavior is related to meso-scale wire damage.

Based in the findings of this research, it is proposed that macro-scale modeling is a justifiable method to capture the mechanical behavior of this woven wire mesh material. The material behavior is in good agreement with elastic modeling, Hill's Analogy, and with Voce hardening. It is noted that the mechanical properties of this material are highly dependent on material orientation, with maxima tending to occur at the main axes.

Funding

Funding for this project was received from the Florida Center for Advanced Aero-Propulsion (FCAAP) Technology.

Acknowledgements

Steven Kraft would like to recognize the assistance of the Honors in the Major undergraduate thesis program in conducting this research. Ali P. Gordon acknowledges the support of a CAE Link Faculty Fellowship. Both authors are thankful for the assistance of Mr. Frank Marinacci with mechanical testing.

References

1. Cavallaro P, Sadegh A and Quigley C. Decrimping behavior of uncoated plain-woven fabrics subjected to combined biaxial tension and shear stresses. *Textile Res J* 2007; 77(6): 404–416.
2. Tarfaoui M and Drean JY. Predicting the stress-strain behavior of woven fabrics using the finite element method. *Textile Res J* 2001; 71(9): 790–795.
3. Nicolleto G and Riva E. Failure mechanisms in twill-weave laminates: FEM predictions vs. experiments. *Composites Part: A* 2004; 35: 787–795.
4. Barbero EJ, Trovillion J, Mayugo JA and Sikkil KK. Finite element modeling of plain weave fabrics from photomicrograph measurements. *Composite Structures* 2006; 73: 41–52.
5. Pierce FT. The geometry of cloth structure. *J Textile Inst* 1936; 28: 45–96.
6. Kawabata S, Niwa M and Kawai H. The finite deformation theories of plain weave fabric Part 1: The biaxial-deformation theory. *J Textile Inst* 1964; 64: 21–46.
7. King M, Jearanaisilawong P and Socrate S. A continuum constitutive model for the mechanical behavior of woven fabrics. *Int J Solids Structures* 2005; 42: 3867–3896.
8. Sun F, Seyam A and Gupta B. A generalized model for predicting load-extension properties of woven fabrics. *Textile Res J* 1997; 67(12): 866–874.
9. Kumazawa H, Susuki I, Morita T and Kuwabara T. Mechanical properties of coated plain weave fabrics under biaxial loads. *Trans Japan Soc Aeronautical Space Sci* 2005; 48(160): 117–123.
10. Chen S, Ding X and Yi H. On the anisotropic tensile behaviors of flexible polyvinyl chloride-coated fabrics. *Textile Res J* 2007; 77(6): 369–374.
11. Voce E. True stress-strain curves and their application to cold-working processes. *Metal Treatment* 1948; 15(54): 53–66.
12. Antoun BR and Song B. Interaction of hydrogen and deformation in 316 L stainless steel. *Proc SEM Annual Conference*, 2009.
13. Gibson RF. *Principles of Composite Material Mechanics*. Boca Raton: CRC Press, 2007, pp. 47–81.
14. Pagano NJ and Halpin JC. Influence of end constraint in the testing of anisotropic bodies. *J Composite Materials* 1968; 2: 18–31.
15. Jones RM. *Mechanics of Composite Materials*. New York: Hemisphere Publishing Co., 1975.
16. Hill R. *The Mathematical Theory of Plasticity*. London: Oxford University Press, 1956, pp. 318–325.
17. Liu P, He G and Wu L. Structure deformation and failure of sintered steel wire mesh under torsion loading. *Materials and Design* 2009; 30: 2264–2268.